

Three-Dimensional Wind-Driven Flow in an Elongated, Rotating Basin

CLINTON D. WINANT

Integrative Oceanography Division, Scripps Institution of Oceanography, University of California, San Diego, La Jolla, California

(Manuscript received 4 March 2003, in final form 13 August 2003)

ABSTRACT

The wind-driven circulation in lakes, lagoons, estuaries, or coastal embayments is described with a linear, steady, three-dimensional barotropic model in an elongated basin of arbitrary depth distribution, on an f plane. With rotation, the vertically averaged velocity scales with the Ekman depth rather than the maximum depth h_0 as in the case without rotation. Near the closed ends of the basin, the flow turns in viscous boundary layers. Because the length of the turning areas depends on the sign of the bottom slope and on δ , the ratio of the Ekman depth to h_0 , there is a striking contrast between the turning areas on either side of an observer looking toward the end of the basin. In the Northern Hemisphere, the turning area on the left is broad, of order $\delta^{-1}B^*$, where B^* is the basin half-width. The turning area on the right is narrow, of order δB^* , and dynamically equivalent to the western boundary current in models of the wind-driven ocean circulation. Ekman solutions are used to describe the vertical structure of the corresponding three-dimensional flow. The axial flow is qualitatively similar to the flow without rotation, but with reduced amplitude. The lateral circulation consists of two superposed gyres. The upper gyre rotates in the sense expected for Ekman transport: the surface flow is to the right of the wind. In the lower gyre, the circulation is in the opposite sense, driven by the veering in the bottom Ekman layer. The largest horizontal and vertical velocities occur in the narrow boundary layer near the end of the basin. Near midbasin, fluid parcels spiral downwind in a sheath surrounding a central core that rotates in the lateral plane, in the sense expected from Ekman dynamics. After turning at the end of the basin, some parcels travel upwind in the central core, while others return in the lower gyre.

1. Introduction

Winds, tides, and buoyancy drive the circulation in small bays, lagoons, or estuaries, and that circulation controls the exchange with the adjacent ocean. With few exceptions, models and analyses of observations of flows in small semienclosed basins have ignored the effect of the earth's rotation. The central objective of this work is to show how rotation can modify the wind-driven flow in these basins. The lateral variability of the wind-driven circulation in an elongated lake was described by Csanady (1973), who developed a solution to the vertically integrated transport equations driven by wind blowing along the axis of the basin, valid away from the basin ends. That solution shows that the transport is downwind near the shallow sides and upwind, driven by an axial pressure gradient, in the deeper channels. Wong (1994) has given solutions for the lateral structure of the flow in a long estuary driven by buoyancy, wind stress, and atmospheric forcing. Mathieu et al. (2002) consider the wind-driven flow in an elongated closed basin and show explicitly how the flow turns

near the axial ends of the basin, over an along-channel distance comparable to the width of the basin.

None of those models consider the effect of the earth's rotation. Pritchard (1967) noted that the Coriolis acceleration was the primary cause for transverse circulation in estuaries, a view that, as noted by Friedrichs and Hamrick (1996), has persisted in the review literature. It is certainly understood that the earth's rotation has to be included in models of circulation in lakes (Simons 1980) and semienclosed seas (Hendershott and Rizzoli 1976). Simons (1980) shows that the structure of the wind-driven flow in a lake depends on the Ekman number, a measure of the importance of friction relative to the Coriolis acceleration. Near midbasin, the axial flow is similar to the flow without rotation, and the lateral flow consists of a near-surface Ekman drift, a drift in the bottom boundary layer associated with the axial current, and a weaker transport associated with the interior inviscid lateral flow. Kasai et al. (2000) and Valle-Levinson et al. (2003) describe the effect of rotation on buoyancy-driven flows in small bays, based on solutions to the Ekman problem with the constraint that the lateral and axial barotropic pressure gradients are constant. As the effect of rotation increases, lateral flows driven by the Coriolis acceleration develop, and for large rotation the vertical structure consists of an

Corresponding author address: Clinton D. Winant, Integrative Oceanography Division, Scripps Institution of Oceanography, University of California, San Diego, 9500 Gilman Drive, La Jolla, CA 92093-0209.
E-mail: cdw@coast.ucsd.edu

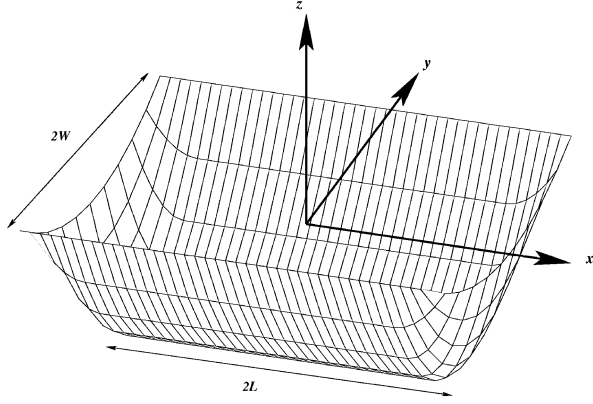


FIG. 1. The coordinate system.

interior that is distinct from the surface and the bottom boundary layers.

The results of Kasai et al. (2000) depend on the assumption of constant axial and lateral pressure gradients. Overall constraints of this type are frequently invoked (Csanady 1973; Simons 1980) to evaluate the pressure gradient required to solve the momentum equations, near the center of a long basin. Pedlosky (1974) points out that in general the pressure field is determined by conditions within the entire basin, and that idea motivates the analysis presented here. The wind-driven circulation in a well-mixed basin is described with a linear barotropic model on an f plane. Coastal lagoons, inverse estuaries, or small bays are idealized as one-half of the closed basin, with the boundary between the lagoon and the ocean at the midpoint of the axis of the model basin. The three-dimensional velocities are derived in two steps. First the vertically integrated vorticity equation is solved for the transport streamfunction and the pressure field throughout the basin. The model of vertically integrated circulation in a closed basin that is developed here bridges the gap between theories that ignore rotation (Mathieu et al. 2002) and theories in which rotation is several orders of magnitude greater than friction (Welander 1968, 1976; Hendershott and Rizzoli 1976). The transport streamfunction is used to evaluate the pressure gradient. The horizontal velocities are then computed from the Ekman solutions, and the vertical velocity is found by integrating the continuity equation. The model demonstrates that even moderate rotation profoundly influences the wind-driven circulation, notably the character and complexity of fluid parcel trajectories. The solutions described are expected to be valid when the wind forcing is steady over periods longer than a day, when the topography changes relatively smoothly, and when relative vertical density differences are less than 10^{-3} .

2. The model

Consider an elongated closed basin on an f plane (Fig. 1). The length is $2L^*$ and the width is $2B^*$. The

origin of the coordinate system is at the center of the at-rest surface. The x coordinate runs along the central axis, y is to the left, and z is measured positive up from the undisturbed surface. Here \mathbf{u}^* is the horizontal velocity vector and w^* is the vertical velocity. The depth is $h^*(x, y)$ and the maximum depth is h_0 . A semienclosed basin, or a lagoon or estuary open to the ocean at one end, corresponds to either half of the closed basin, with the open end at $x = 0$. The constant-density fluid is driven by a steady wind stress vector $\tau_s(x, y)$, and η^* is the position of the surface relative to $z = 0$. The vertical eddy viscosity is K . Under these conditions, the linearized equations of motion are

$$\nabla^* \cdot \mathbf{u}^* + w_{z^*}^* = 0 \quad \text{and}$$

$$f\mathbf{k} \times \mathbf{u}^* = -g\nabla^* \eta^* + K \frac{\partial^2 \mathbf{u}^*}{\partial z^{*2}}, \quad (1)$$

with boundary conditions

$$\mathbf{u}_{z^*}^* = \frac{\tau_s}{\rho K} \quad \text{and} \quad w^* = 0 \quad \text{at} \quad z^* = 0 \quad \text{and} \quad (2)$$

$$\mathbf{u}^* = 0 \quad \text{and} \quad w^* = 0 \quad \text{at} \quad z^* = -h^*. \quad (3)$$

Lateral mixing is ignored because the ratio of vertical to horizontal dimensions is assumed to be very small. As a consequence, the only boundary condition imposed on the flow at the basin edges is that the normal velocity be zero or, equivalent, that the streamfunction be constant on those boundaries.

Dimensional (starred) variables are related to non-dimensional (unstarred) variables as

$$(x, y, L) = \frac{(x^*, y^*, L^*)}{B^*}, \quad z = z \frac{z^*}{h_0}, \quad h = \frac{h^*}{h_0}, \quad (4)$$

$$\mathbf{u} = \frac{\rho K \mathbf{u}^*}{|\tau_s| h_0}, \quad w = \frac{\rho B^* K w^*}{|\tau_s| h_0^2}, \quad \text{and}$$

$$\eta = \frac{\rho g h_0 \eta^*}{|\tau_s| B^*}, \quad (5)$$

and the nondimensional equations of motion become

$$\nabla \cdot \mathbf{u} + w_z = 0 \quad \text{and}$$

$$\frac{2}{\delta^2} \mathbf{k} \times \mathbf{u} = -\nabla \eta + \frac{\partial^2 \mathbf{u}}{\partial z^2}, \quad (6)$$

where the nondimensional Ekman depth is defined as $\delta = [(2K)/(fh_0^2)]^{1/2}$. Here δ^{-1} , the ratio of the maximum depth to the dimensional Ekman depth, is taken in the remainder as an index of the importance of rotation, and δ is related to the usual definition of the Ekman number $E = K/fh_0^2$ by $\delta = (2E)^{1/2}$.

3. Ekman solutions and bottom stress formulation

The vertical distribution of velocity is governed by the balance among vertical stress divergence, pressure

gradients, and the Coriolis acceleration, as in the Ekman-layer solutions. If u and v are the components of \mathbf{u} , $V = u + iv$, and $N = \eta_x + i\eta_y$, Eq. (6) becomes

$$\frac{d^2V}{dz^2} - \frac{2i}{\delta^2}V = N, \quad (7)$$

with boundary conditions

$$V_z = t_s \quad \text{at } z = 0 \quad \text{and} \quad V = 0 \quad \text{at } z = -h, \quad (8)$$

where $t_s = t_s^x + it_s^y$ is the direction of the wind stress in the complex plane. With $\alpha^2 = 2i\delta^{-2}$, the solution of Eq. (7) subject to Eq. (8) is

$$V = t_s \frac{\sinh[\alpha(z+h)]}{\alpha \cosh(\alpha h)} - \frac{N}{\alpha^2} \left[1 - \frac{\cosh(\alpha z)}{\cosh(\alpha h)} \right]. \quad (9)$$

The vertically integrated transport is

$$[V] = \int_{-h}^0 V dz = t_s h^2 \frac{\cosh(\alpha h) - 1}{(\alpha h)^2 \cosh(\alpha h)} + Nh^3 \frac{\tanh(\alpha h) - \alpha h}{(\alpha h)^3}, \quad (10)$$

and the nondimensional bottom stress T_b is

$$T_b = \frac{dV}{dz} \Big|_{z=-h} = \frac{t_s}{\cosh(\alpha h)} - Nh \frac{\tanh(\alpha h)}{\alpha h} \quad (11)$$

or, eliminating t_s between Eqs. (10) and (11),

$$T_b = (F_1 + iF_2) \frac{[V]}{h^2} + (G_1 + iG_2)Nh, \quad (12)$$

where

$$\begin{aligned} F_1 &= \text{Re} \left[\frac{(\alpha h)^2}{\cosh(\alpha h) - 1} \right], \\ F_2 &= \text{Im} \left[\frac{(\alpha h)^2}{\cosh(\alpha h) - 1} \right], \\ G_1 &= -\text{Re} \left[\frac{\tanh(\alpha h) - \alpha h}{\cosh(\alpha h) - 1} + \tanh(\alpha h) \right], \quad \text{and} \\ G_2 &= -\text{Im} \left[\frac{\tanh(\alpha h) - \alpha h}{\cosh(\alpha h) - 1} + \tanh(\alpha h) \right]. \end{aligned} \quad (13)$$

The F_s give the amplitude of the bottom stress driven by the vertically averaged flow, and the G_s give the amplitude of the bottom stress driven by the pressure gradient. These functions all depend on $\delta^{-1}h$, and that dependence is illustrated in Fig. 2. For small $\delta^{-1}h$, $F_1 = 2$, $G_1 = -1/3$, and both F_2 and G_2 are zero. For large $\delta^{-1}h$, F_1 and F_2 both tend to zero, $G_1 = -\delta/2h$, and $G_2 = \delta/2h$. Three different regimes can be defined based on Fig. 2. The case with no rotation corresponds to $\delta^{-1}h = 0$. For $\delta^{-1}h > 10$, both F_1 and F_2 are practically zero, and the bottom stress is a function of $\nabla\eta$ alone, as in the classic oceanic models (Stommel 1948; We-

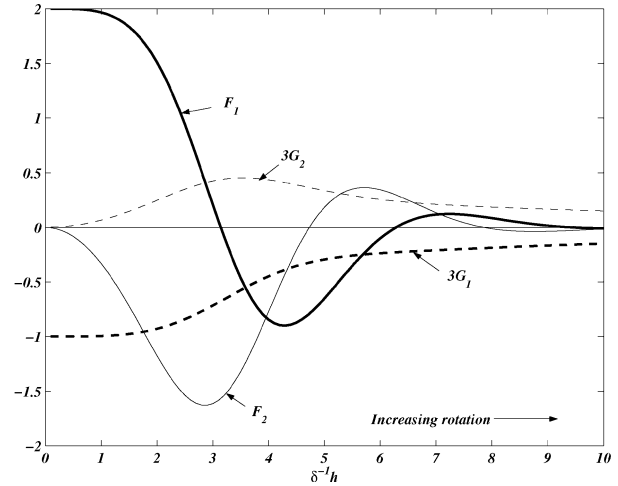


FIG. 2. Dependence of bottom stress coefficients on $\delta^{-1}h$.

lander 1968, 1976). Rotation begins to modify the flow in the intermediate range, $0 < \delta^{-1} < 10$, that is the central focus of this paper.

4. The vertically integrated flow

With the transport streamfunction ψ defined as

$$\psi_x = \int_{-h}^0 v dz \quad \text{and} \quad \psi_y = - \int_{-h}^0 u dz, \quad (15)$$

or

$$\mathbf{U} = \mathbf{k} \times \nabla\psi, \quad (16)$$

the vertically integrated form of Eq. (6) is

$$2\delta^{-2}\nabla\psi = h\nabla\eta - \mathbf{t}_s + \mathbf{T}_b, \quad (17)$$

where \mathbf{t}_s is a unit vector in the direction of the wind stress. In vector notation, the bottom stress as given by Eq. (12) is

$$\begin{aligned} \mathbf{T}_b &= h^{-2}(F_1\mathbf{k} \times \nabla\psi - F_2\nabla\psi) \\ &\quad + h(G_1\nabla\eta + G_2\mathbf{k} \times \nabla\eta). \end{aligned} \quad (18)$$

This expression for the bottom stress distinguishes this model from that proposed by Mathieu et al. (2002) in which rotation is ignored and from the bottom stress parameterization used by Welander (1968) in which the bottom stress is a function of the geostrophic flow only. With Eq. (18) the momentum Eq. (17) becomes

$$\begin{aligned} 2\delta^{-2}\nabla\psi &= h[(1 + G_1)\nabla\eta + G_2\mathbf{k} \times \nabla\eta] \\ &\quad + h^{-2}(F_1\mathbf{k} \times \nabla\psi - F_2\nabla\psi) - \mathbf{t}_s. \end{aligned} \quad (19)$$

By noting that $\mathbf{k} \times \mathbf{k} \times \nabla\eta = -\nabla\eta$, Eq. (19) can be solved for $\nabla\eta$:

$$\nabla\eta = -\delta^{-1}S\nabla\psi - R\mathbf{k} \times \nabla\psi + \frac{\mathbf{t}_s}{Ph} - \mathbf{k} \times \frac{Q\mathbf{t}_s}{Ph}, \quad (20)$$

where

$$Q = \frac{G_2}{1 + G_1}, \quad P = 1 + G_1 + QG_2, \quad (21)$$

$$S = \frac{\delta}{Ph^3} \left(QF_1 - 2\frac{h^2}{\delta^2} - F_2 \right), \quad \text{and}$$

$$R = \frac{F_1}{Ph^3} + \frac{Q}{Ph^3} \left(2\frac{h^2}{\delta^2} + F_2 \right), \quad (22)$$

η can be eliminated by taking the curl of Eq. (20) to give a vorticity equation:

$$\nabla \cdot R \nabla \psi + \delta^{-1} \nabla S \times \nabla \psi = \nabla \times \frac{\mathbf{t}_s}{Ph} - \nabla \cdot \frac{Q \mathbf{t}_s}{Ph}. \quad (23)$$

If the depth only varies as a function of lateral position, $h = h(y)$, and the wind stress is constant and parallel to the axis of the basin (\mathbf{t}_s is the unit vector in the x direction). Eq. (23) becomes

$$\nabla^2 \psi + \frac{R_y}{R} \psi_y - \delta^{-1} \frac{S_y}{R} \psi_x = -\frac{1}{R} \left(\frac{1}{Ph} \right)_y. \quad (24)$$

In the limit of no rotation ($Q = 0$, $P = 2/3$, $R = 3h^{-3}$, and $S = 0$), Eq. (24) reduces to

$$\nabla \cdot \frac{2}{h^3} \nabla \psi = -\left(\frac{1}{h} \right)_y, \quad (25)$$

which was solved by Mathieu et al. (2002). Away from the axial boundaries, the solution corresponds to that presented by Csanady (1973), with downwind flow where h is small and upwind flow in the deeper areas. Near the axial boundaries, the vertically integrated flow turns around in regions of length comparable to the width of the basin.

When rotation is important, δ^{-1} is large and $Q \rightarrow \delta/2h$, $P \rightarrow 1$, $R \rightarrow 2/\delta h^2$, and $S \rightarrow -4/\delta h$. In this limit Eq. (24) becomes

$$\nabla^2 \psi - 2\frac{h_y}{h} \psi_y - 2\frac{h_y}{\delta} \psi_x = \delta h_y. \quad (26)$$

This expression is the same as the vorticity equation derived by Welander (1968) and Hendershott and Rizoli (1976), the latter in the case of wind forcing only. It is also similar to the equation derived by Stommel (1948) to model the wind-driven circulation of the ocean. The effect of varying latitude in that problem plays a similar role to the effect of varying depth in the problem considered here. The factor δ on the right-hand side means that for large rotation rates the streamfunction scales as δ , and it suggests the introduction of $\psi^r = \delta^{-1} \psi$.

5. Analytic solution in a rectangular basin

Equation (24) can be solved analytically, for finite $\delta > 1$, when the sign of the bottom slope does not change. Consider a rectangular basin of length $2L$ and width 1.

The depth decreases from $y = 0$ to $y = 1$ where it is zero. Here h_y is negative. The wind stress is uniform and in the axial direction. In terms of ψ^r the vorticity Eq. (24) is

$$\psi^{r_{xx}} - \delta^{-1} \frac{S_y}{R} \psi^r_x + \psi^{r_{yy}} + \frac{R_y}{R} \psi^r_y = -\frac{1}{\delta R} \left(\frac{1}{Ph} \right)_y, \quad (27)$$

with the boundary condition that $\psi^r = 0$ on the sides of the basin. The factors R_y/R , S_y/R , and $1/\delta R$ all remain finite as $\delta^{-1} \rightarrow \infty$.

The geometry is similar to that considered by Welander (1976), and, as in that model, it is convenient to think of the domain as consisting of three parts: a central section that corresponds to the zonally uniform regime in the Welander (1976) model and two end regions that have distinct lateral scales and distinct dynamics.

a. Solution near the middle of the basin

Away from axial boundaries ($|x| \ll L$), in the part of the basin described by Csanady (1973) as the ‘‘trunk’’ section, $\partial/\partial x \approx 0$ and Eq. (27) becomes

$$\psi^{r_{yy}} + \frac{R_y}{R} \psi^{r_y} = -\frac{1}{\delta R} \left(\frac{1}{Ph} \right)_y. \quad (28)$$

This equation differs from the equation that governs the zonally uniform regime in the Welander (1976) model because of the inclusion of the second term on the right-hand side that accounts for variations of the depth in the lateral (y) direction.

Equation (28) can be integrated once, and the axial transport is

$$\psi^{r_{y,i}} = \frac{1}{\delta R} \left[\frac{\langle (RPh)^{-1} \rangle}{\langle R^{-1} \rangle} - \frac{1}{Ph} \right], \quad (29)$$

where $\langle \rangle$ denotes the average value across the width of the basin. The constant of integration is evaluated by requiring $\psi^{r,i} = 0$ on $y = 0, 1$, or, equivalent, that there be no net axial transport across any section ($\langle \psi^{r,i} \rangle = 0$). Here $\psi^{r,i}$ is illustrated in Fig. 3 for a linearly sloping bottom, for different values of δ^{-1} . This solution has the same general form as the solution to the nonrotating problem that has been extensively discussed by Csanady (1973) and others. It represents downwind flow (negative $\psi^{r,i}$) in the shallow areas near the lateral boundaries, directly driven by the wind stress, and an upwind return flow (positive $\psi^{r,i}$) in the deeper areas, driven by the pressure gradient required to satisfy the no-net-axial-transport condition. For small δ^{-1} , the dimensional transport is proportional to $\tau_s h_0^2 / (\rho K)$. As δ^{-1} increases, the dimensional transport becomes proportional to $\tau_s h_0 \delta / (\rho K)$. For any value of δ^{-1} , there is always a shallow area (y near 1) where the axial momentum balance is between surface and bottom stress (Couette flow). The width of that area diminishes as rotation increases and, as shown in Fig. 3, the lateral location

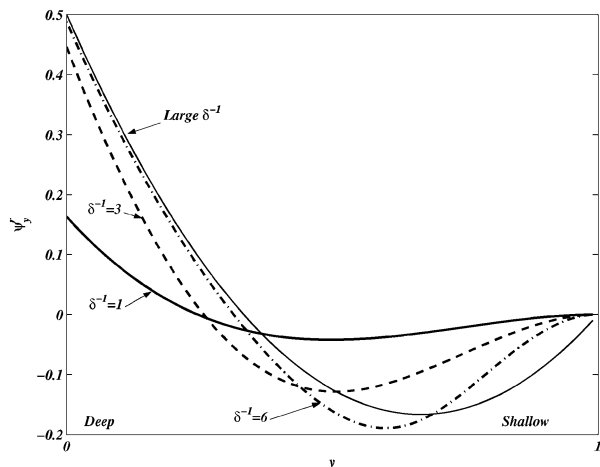


FIG. 3. Plot of ψ_y as a function of lateral position for different values of δ^{-1} , for a positive wind stress, near the middle of the basin. The depth decreases from $y = 0$ to zero at $y = 1$. The vertically integrated flow is upwind (positive ψ_y) in the deeper areas (near $y = 0$) and in the opposite direction in the shoal areas.

of maximum downwind transport moves into shallower depths.

b. Midbasin momentum balance

The vertically integrated momentum balances provide further insight into the midbasin flow. Near the middle of the basin, axial gradients (except for the axial pressure gradient) are negligible, and, in particular, the lateral transport ψ_x^r is zero (straight flow) for all y . In this limit, Eq. (17) reduces to

$$h\eta_x + T_b^x = 1 \quad \text{and} \quad \delta\eta_y + \delta T_b^y = 2\psi_y^r. \quad (30)$$

Because the flow does not depend on x , the lateral

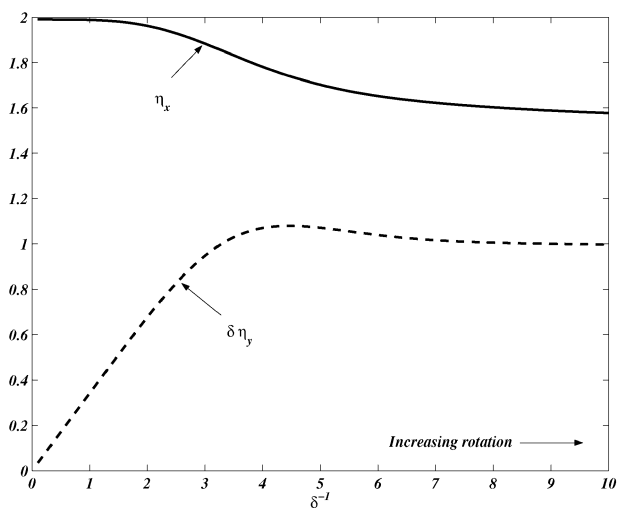


FIG. 4. Axial and lateral pressure gradients at the deepest point of a rectangular basin driven by axial wind stress, as a function of δ^{-1} . The depth is a linear function of y .

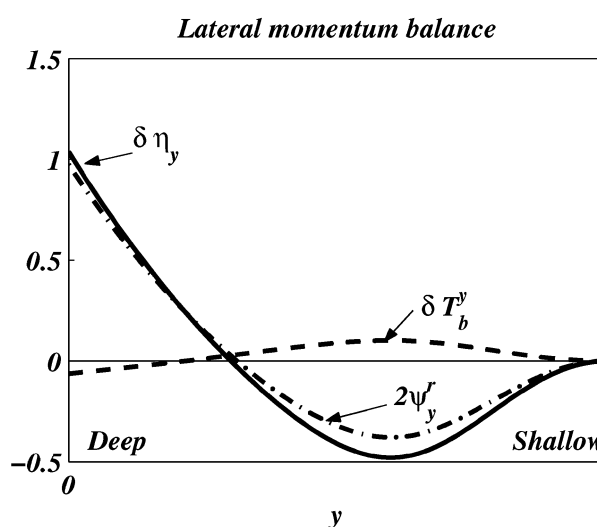
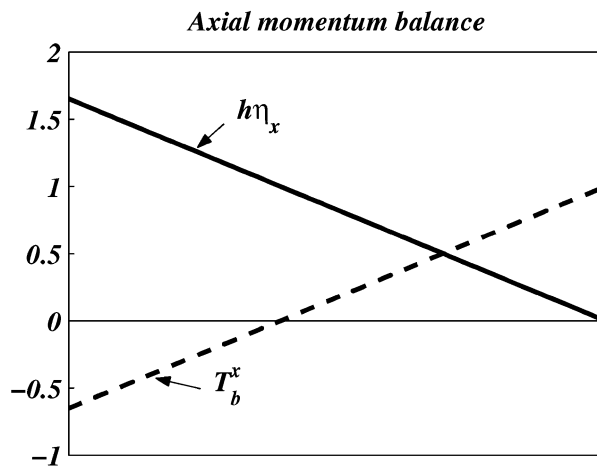


FIG. 5. Terms in the vertically integrated (top) axial and (bottom) lateral momentum balance, away from axial ends, for $\delta^{-1} = 6$. The depth decreases from $y = 0$ to zero at $y = 1$.

momentum equation imposes the condition that η_y can only be a function of y . Then the axial gradient η_x can only be a function of x . The axial gradient (constant across the width of the basin), and the maximum value of the lateral gradient (at the deepest point of the section) are illustrated in Fig. 4, as a function of the rotation parameter δ^{-1} . The axial gradient decreases from $2\tau_s/(\rho gh_0)$ to $1.5\tau_s/(\rho gh_0)$ with increasing rotation. Without rotation, the lateral gradient is zero. It increases to $\tau_s/(\rho g\delta)$ when $\delta^{-1} > 6$.

Lateral profiles of the terms in Eq. (30) are illustrated in Fig. 5. In the axial balance, the axial component of the bottom stress and the product $h\eta_x$ add up to equal the surface stress. The magnitude of the lateral component of the bottom stress is comparable to the axial component but is smaller than the remaining two terms in the lateral momentum balance: the Coriolis acceleration associated with the lateral transport and the lateral pressure gradient. The scaling shows that as rotation

increases, terms in the vertically integrated lateral momentum become progressively larger than their counterparts in the axial equation.

c. Solutions near the ends

To satisfy the boundary condition at an axial boundary, either one or both of the first two terms in Eq. (27) need to be retained. Without rescaling x , the second term on the left becomes dominant as δ^{-1} becomes large, corresponding to zero lateral velocity, a solution without physical meaning near a boundary, where the flow turns. Two other scalings are possible.

1) BOUNDARY LAYER AT $x = L$: THE SVERDRUP FLOW

With $x^+ = \delta x$, corresponding to a turning area of dimensional length $\delta^{-1}B^*$, as δ^{-1} becomes large, Eq. (27) reduces to

$$\frac{S_y}{R} \psi_{x^+}^{r,+} - \psi_{yy}^{r,+} - \frac{R_y}{R} \psi_y^{r,+} = \frac{1}{\delta R} \left(\frac{1}{Ph} \right)_y. \quad (31)$$

For $h_y < 0$, S_y/R is negative, in which case this end region will be located near $x = L$. The boundary conditions accordingly are

$$\begin{aligned} \psi^{r,+} &= 0 & \text{at } x^+ &= \delta L \quad \text{and} \\ \psi^{r,+} &\rightarrow \psi^{r,i} & \text{as } \delta L - x^+ &\rightarrow \infty. \end{aligned} \quad (32)$$

This end region corresponds to the Sverdrup boundary layer, in the terminology of the Welander (1976) model. The vorticity balance is the same as is normally described for the ‘‘interior’’ in ocean circulation models, that is, a balance between the Sverdrup transport [the first term on the left-hand side of Eq. (31)], the lateral frictional terms, and the forcing. The equation is parabolic and is similar to the streamfunction equation for the arrested topographic wave solution described by Csanady (1978). In the appendix, the solution of Eq. (31) is shown to be

$$\psi^{r,+} = \sum_{n=0}^{\infty} a_n Y_n(y) [1 - e^{\lambda_n \delta(x-L)}], \quad (33)$$

where the λ_n and Y_n are the eigenvalues and eigenvectors of Eq. (A2) and the a_n are given by Eq. (A6).

The eigenvalues λ_n are positive for $h_y < 0$ as shown in the appendix. The solution in Eq. (33) is zero at $x = L$ and increases toward $\psi^{r,i}$ away from that boundary. The solution is approximately $(1 - e^{-1})\psi^{r,i}$ at a distance $x = (\lambda_1 \delta)^{-1}$ from the boundary. Because $\lambda_1 \approx 10$, the physical length of this turning area is about $\delta^{-1}/10$.

2) BOUNDARY LAYER AT $x = -L$: THE STOMMEL LAYER

For Eq. (27), the second choice of scaling is $x^- = \delta^{-1}x$, when, as δ^{-1} becomes large, the vorticity Eq. (27) reduces to

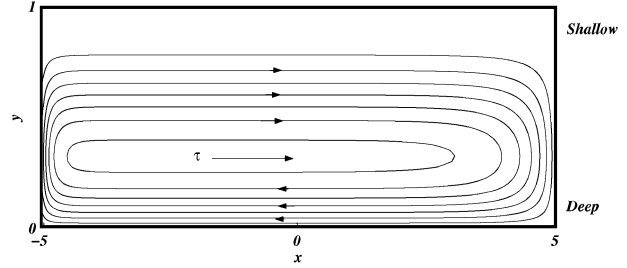


FIG. 6. The transport streamfunction ψ^r for the analytic solution to Eq. (27) for $\delta^{-1} = 6$. The depth is $h = 1 - y$. The wind stress is applied in the $+x$ direction. The streamfunction is zero on the boundaries. The Sverdrup end region is on the right.

$$\psi_{x^- x^-}^{r,-} - \frac{S_y}{R} \psi_{x^-}^{r,-} = 0. \quad (34)$$

This equation is the same as proposed by Stommel (1948) for the Gulf Stream, and so it is appropriate to call this the Stommel boundary layer. For $h_y < 0$, the boundary conditions to be satisfied are $\psi^{r,-} = 0$ at $x = -L$, and $\psi^{r,-} = \psi^{r,i}$ far from the boundary. The solution of Eq. (34) is

$$\psi^{r,-} = [1 - e^{S_y(x+L)/\delta R}] \psi^{r,i}. \quad (35)$$

This solution is the equivalent to the solution for the western boundary current in the wind-driven ocean circulation problem (Stommel 1948). Here $x + L$ is always positive and $S_y/R < 0$ when $h_y < 0$, and so the exponent is negative. When δ^{-1} is large, $S_y/R \approx 2h_y$ and the solution is $(1 - e^{-1})\psi^{r,i}$ at a distance $x = \delta/2 |h_y|$ from the boundary. The turning area is narrow, and the transports are consequently large. Within this zone, the dimensional horizontal velocity is of order $|\tau_s| h_0 / (\rho K)$, independent of the rotation rate.

The full solution of Eq. (27) for the vertically integrated streamfunction in an elongated rotating basin that extends from $x = -L$ to L and from $y = 0$ to $y = 1$, when $h_y < 0$ and $\delta^{-1} > 1$, is thus

$$\psi^r = [1 - e^{S_y(x+L)/\delta R}] \sum_{n=0}^{\infty} a_n Y_n(y) [1 - e^{\lambda_n \delta(x-L)}]. \quad (36)$$

This solution is illustrated in Fig. 6 for $\delta^{-1} = 6$, in a basin where $L = 5$ and the depth decreases linearly from $y = 0$ to $y = 1$. The height of the Ekman layer is about 3δ , and thus $\delta^{-1} = 6$ corresponds to the condition in which the surface and bottom Ekman layers just begin to be distinct. The streamline pattern is similar to simple models of ocean circulation, with a broad region in Sverdrup balance on the right, a narrow Stommel boundary layer characterized by large vertically integrated velocities on the left, and a laterally uniform region in between. Details of the circulation pattern are different, however, for two reasons. The first is related to the formulation of the bottom stress [Eq. (18)], which depends on both the surface stress (through the F terms) and on the pressure gradient (through the G terms). The

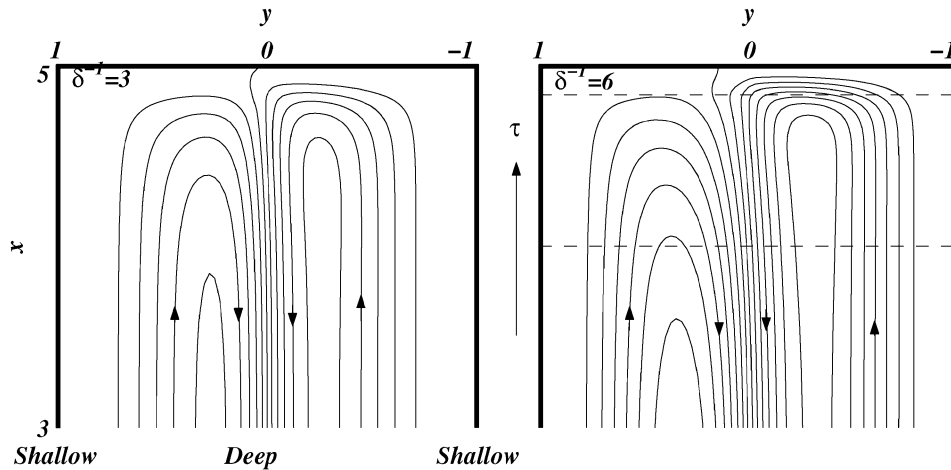


FIG. 7. The transport streamfunction $h_0\psi/\delta$ for the solution to Eq. (23) for $\delta^{-1} = 3$ and 6. Here $L = 5$ and $h = 1 - |y|$ except within a distance of 0.25 from the ends, where the bottom shoals to zero. Only the end of the basin, between $x = 3$ and 5, is shown. The wind stress is applied in the $+x$ direction. The contour interval is 0.01, and the streamfunction is zero on the boundaries. The two dashed lines in the right-hand panel denote the location of the sections illustrated in Fig. 13.

second reason is related to the wind stress that sets up an axial pressure gradient, as is shown in the vertically integrated axial momentum balance [Eq. (30)].

6. More complicated basin shapes

The solution described in the previous section is limited to the case in which the depth only depends on lateral position and the bottom slope does not change sign, conditions that are not met in most of the semienclosed basins of interest here. In this section, solutions for more realistic basin shapes are described, based on numerical solutions to Eq. (23), evaluated using Gauss–Seidel iteration (Fausett 1999). For simplicity, the wind stress is still considered to be constant and aligned with the x axis.

A rectangular basin extending from $y = -1$ to $y = 1$, with $L = 5$, is considered first. The depth is a linear function of lateral position ($h = 1 - |y|$), except in a small region (of length 0.25) near $|x| = L$, where the depth shoals to zero. Streamfunctions for two different values of δ^{-1} are illustrated in Fig. 7 for the positive x end of the basin. The left side of each frame, corresponding to positive values of y , is the Sverdrup boundary layer, similar to the right side of Fig. 6: the vertically integrated flow turns in a broad region whose width increases with increasing rotation. For negative y , in the Stommel boundary layer, the width of the turning region decreases with increasing rotation, corresponding to the left side of Fig. 6.

In the area illustrated in Fig. 7, the central streamline moves away from $y = 0$ near the boundary. This region is where the flow in the Sverdrup boundary layer on the left and in the Stommel boundary layer on the right have to adjust. This adjustment area is similar to the internal boundary layers that Welander (1968) has de-

scribed in the vicinity of locations where the bottom slope changes sign.

Most estuaries and lagoons shoal gradually in both the lateral and axial directions. The second basin considered is similar to the first, but the bottom shoals to zero depth over an axial distance equal to 2. The streamfunction and bottom contours are illustrated in Fig. 8, for $\delta^{-1} = 6$. They are qualitatively similar to the pattern in Fig. 7. The shoaling bottom lengthens the turning areas, because the increased effect of friction associated with the smaller depth reduces the magnitude of the transport. Even so, the turning areas in regions of positive and negative bottom slope are very different.

Estuaries and coastal lagoons are often elongated, but many bays are not, and the question arises as to what the wind-driven flow in a rotating square basin looks like. Equation (23) has been solved for a closed square basin in which the depth is maximum at the center and tapers off toward the sides. The solution is illustrated in Fig. 9. The vertically integrated flow consists of two counterrotating gyres, and the essential features of the solutions described above are retained. These solutions are very similar to the streamfunctions computed by Birchfield (1967) for the horizontal transport in a rotating parabolic basin, driven by a uniform wind stress.

7. Three-dimensional structure

Given ψ , or equivalently given η , the horizontal velocity can be computed from Eq. (9), and the vertical velocity is derived by integrating the continuity equation down from the surface, where $w = 0$. Near midbasin, the streamfunction and sea level are determined by Eq. (29), and the local velocities are determined analytically. In the end regions, the three local velocities are determined from the numerical solutions for ψ .

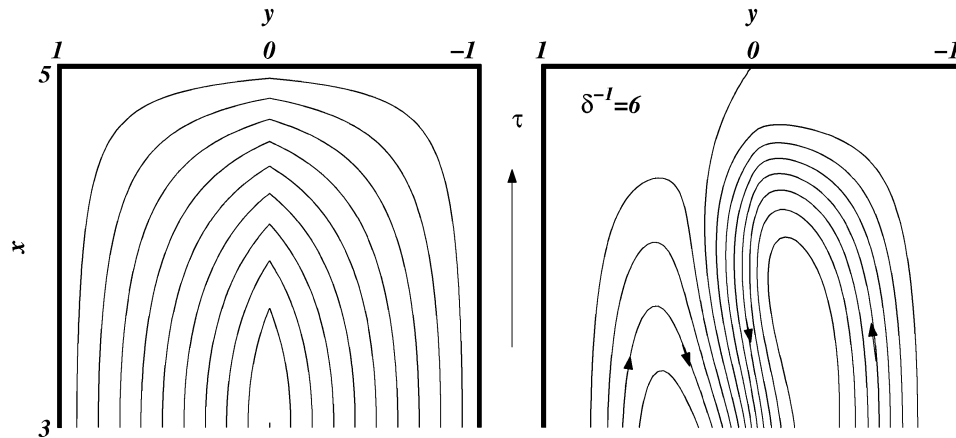


FIG. 8. (left) Bathymetry and (right) transport streamfunction for the solution to Eq. (23) for $\delta^{-1} = 6$. The basin geometry is the same as for Fig. 7 except that the bottom shoals toward the ends over an axial distance equal to 2. The wind stress is applied in the $+x$ direction. The contour interval is 0.01, and the streamfunction is zero on the boundaries.

a. The flow near the middle of the basin

Velocity sections located at the midpoint of the basin ($x = 0$) are illustrated in Fig. 10, for different values of the rotation parameter δ^{-1} . General features of these solutions are as follows. Because the depth shoals to zero gradually, there is always an area near the sides of the basin where the surface and bottom stress balance, and the axial flow is downwind. If the basin is closed, the axial transport in any lateral section must be zero, and the downwind flow on the sides is balanced by an upwind flow in the deeper areas. This pattern holds for any depth distribution, except if the depth is constant (rectangular section). The lateral circulation is to the right of the wind at the surface and near the bottom, with a compensating return flow in the interior. The overall lateral circulation, consisting of two counter-rotating gyres, is similar to the flow described by Simons (1980). If one looks in the direction of the wind stress, the near-surface gyre rotates in the clockwise direction

in the Northern Hemisphere, consistent with Ekman transport to the right of the wind stress. The lower gyre rotates in the opposite sense and is driven by veering in the bottom Ekman layer.

For $\delta^{-1} = 1$, the axial velocity distribution is nearly unchanged from the results of Wong (1994) for the case without rotation. At this low value of δ^{-1} , the lateral velocities are much smaller than the axial velocities, but the pattern of lateral velocities is as described above. For moderate rotation ($\delta^{-1} = 3$) the distribution of axial velocity remains practically unchanged from the distribution without rotation. The amplitude of the lateral velocity is larger: at the surface and in the middle of the basin, $v \approx 0.05$, an appreciable fraction of the maximum axial velocity $u \approx 0.25$. The axial circulation becomes weaker when rotation becomes relatively large ($\delta^{-1} = 6$), and the location of the maximum downwind velocity moves toward shallower depth, consistent with the similar movement of the axial transport illustrated

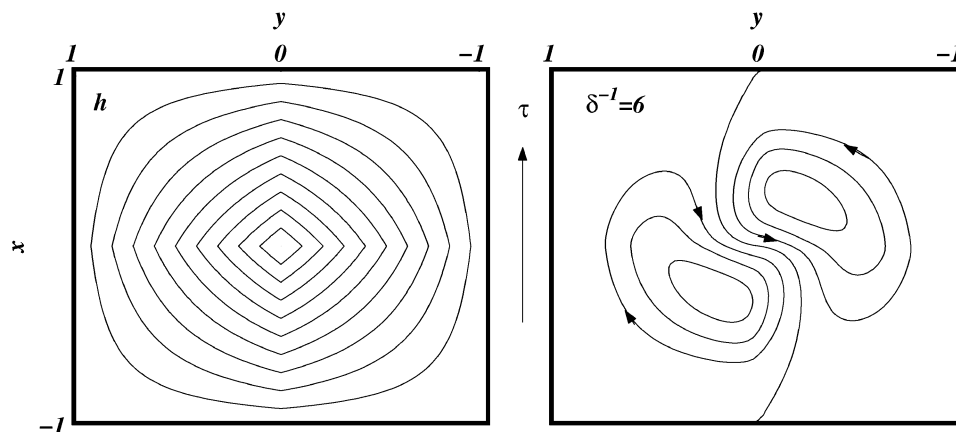


FIG. 9. (left) Bathymetry and (right) transport streamfunction for the solution to Eq. (23) for a square basin. The wind stress is applied in the $+x$ direction. The contour interval is 0.01.

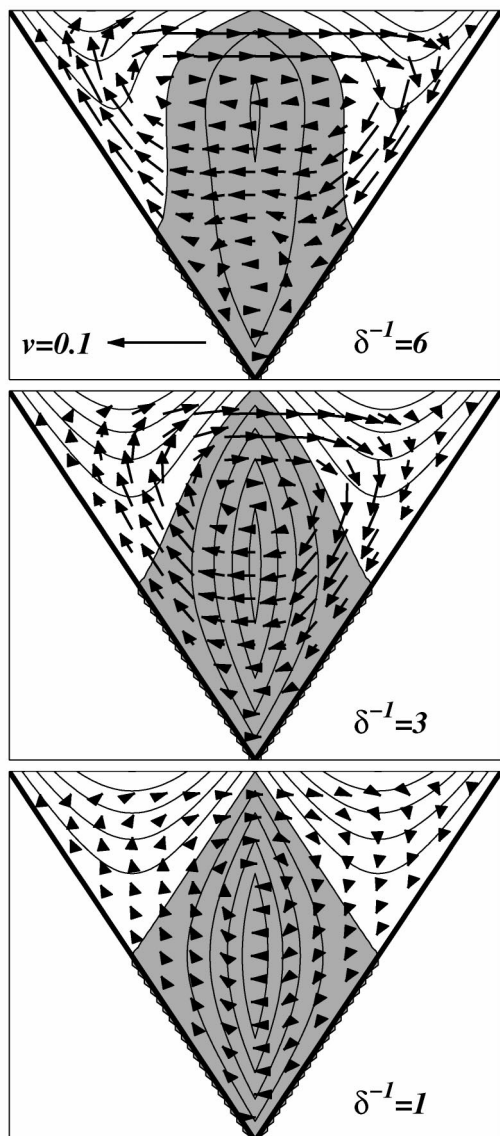


FIG. 10. Velocity sections midway between the basin ends ($x = 0$) for different values of δ^{-1} . The wind stress is applied in the $+x$ direction, and the view is toward positive x . The axial velocity is negative in the shaded areas, and the axial-velocity contour interval is 0.05. Lateral and vertical velocities (v and w) are represented by vectors. The lateral velocity scale is the same for all δ^{-1} .

in Fig. 3. The surface layer becomes distinct in the lateral circulation, and an interior region is apparent throughout the central portion of the section. The up- and downwelling patterns are moved toward the lateral boundaries. The strongest lateral and vertical velocities occur in a sheath around the periphery of the basin.

The three-dimensional solutions presented to this point were all derived for a linear distribution of depth. Velocity sections at the midpoint ($x = 0$) of a basin for parabolic and Gaussian depth profiles are illustrated in Fig. 11. While the bathymetry does control the exact

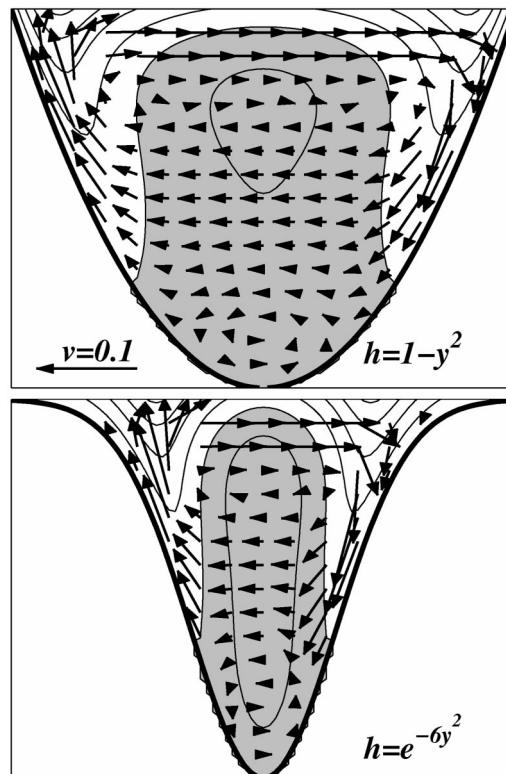


FIG. 11. Velocity sections for $\delta^{-1} = 6$ for (top) parabolic and (bottom) Gaussian depth profiles, at the center, $x = 0$, of the basin ($L = 5$). The axial velocity is negative in the shaded areas, and the axial-velocity contour interval is 0.05. The lateral velocity scale is the same for both frames.

location of flow features, the flows are qualitatively similar for all depth distributions.

b. Midbasin momentum balance

The local momentum balance can be compared with the vertically integrated momentum balance described in section 5. Away from the ends, where the vertically integrated flow is straight, the axial and lateral components of Eq. (6) are

$$-\frac{2}{\delta^2}v = -\eta_x + \frac{\partial^2 u}{\partial z^2} \quad \text{and} \quad \frac{2}{\delta^2}u = -\eta_y + \frac{\partial^2 v}{\partial z^2}, \quad (37)$$

where the left-hand side represents the Coriolis acceleration and the last term on the right-hand side represents the divergence of the stress, or the friction term. Local values of the terms involving the velocity in Eq. (37) are illustrated in Fig. 12. In terms of the axial balance, both the Coriolis and friction terms reach values that exceed the axial pressure gradient by a factor of order δ^{-1} . Terms in the local momentum balance are thus larger than in the vertically integrated equation, by

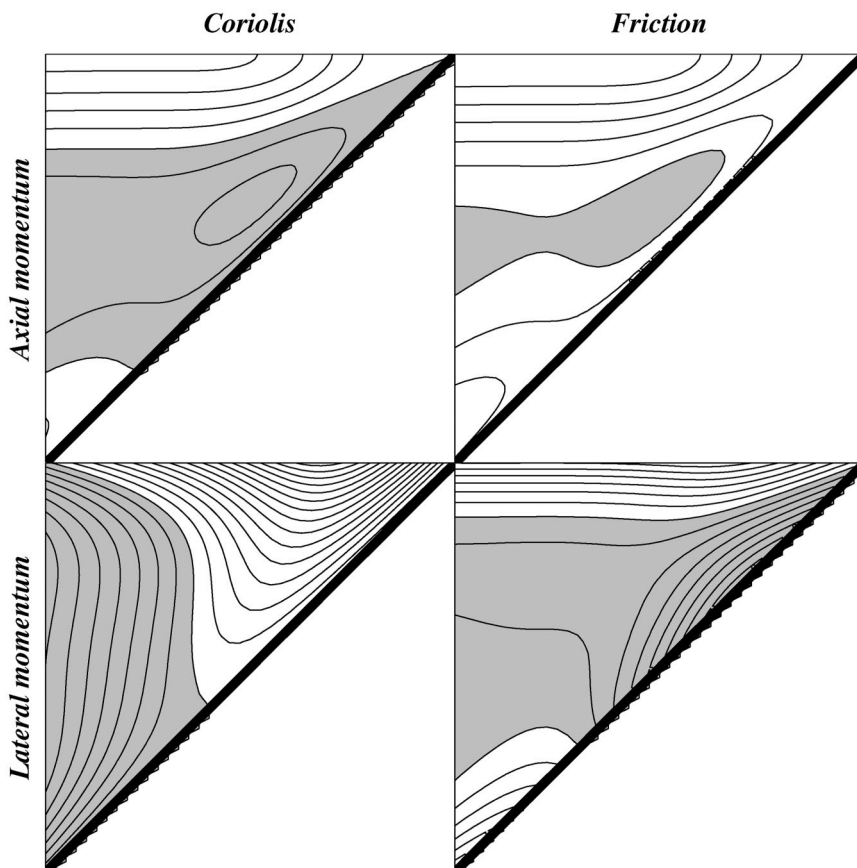


FIG. 12. Components of the local momentum balance near $x = 0$ and between $y = -1$ and $y = 0$ for $\delta^{-1} = 6$. The distribution for positive y is the same as shown here for negative y . Terms in the shaded areas are negative, and the contour interval is 1. The difference between the left and right panels is the negative of the depth-independent pressure gradient illustrated in Fig. 4. The lateral pressure gradient varies as a function of y as illustrated in Fig. 5. At $y = 0$, $\eta_y = \delta^{-1}$, and so the two lower panels differ by -6 in the middle.

the same factor. This result is because the lateral transport is zero, and consequently the vertically integrated axial Coriolis acceleration is zero while the local value is of order δ^{-1} .

The lateral component of the Coriolis acceleration dominates the lateral momentum balance. It changes sign between the edges and the center of the basin where it is negative, because of the upwind (negative) axial flow. Away from the boundaries, the lateral Coriolis acceleration is balanced by the lateral pressure gradient. Near the boundaries, the Coriolis term becomes small because the no-slip boundary condition forces the velocity to zero, and the friction term balances η_y .

c. Solutions near the ends

The velocity patterns near the closed ends are qualitatively different from the patterns near the middle of the basin. Velocity sections at relative distances of 1 and δ from the end (located at $x = L$) are illustrated in Fig. 13, for $\delta^{-1} = 6$. The corresponding velocity section

near the middle of the basin is illustrated in the top frame of Fig. 10. At a distance equal to the basin half-width of the closed end (lower frame of Fig. 13), the axial velocity field has become slightly asymmetric: the area (unshaded) of downwind flow is slightly larger on the right (negative y) side. The depth of the near-surface layer where the lateral flow is negative is greater on the left side. Closer to the end (top frame of Fig. 13), at a relative distance comparable to the width of the narrow turning area, all the velocity patterns are different from those discussed to this point. The axial velocity is organized in horizontal layers, with downwind flow near the surface overlying weak upwind flow. The lateral velocities are larger than in any other part of the basin and are larger on the right (negative y) side, where the vertically integrated flow is toward the center of the basin. On the left side, the lateral flow is weaker, which is consistent with the more gradual turning process associated with the broader turning area. Except near the core of the basin, the vertical velocities are negative, and they are larger on the right side. Fluid coming from

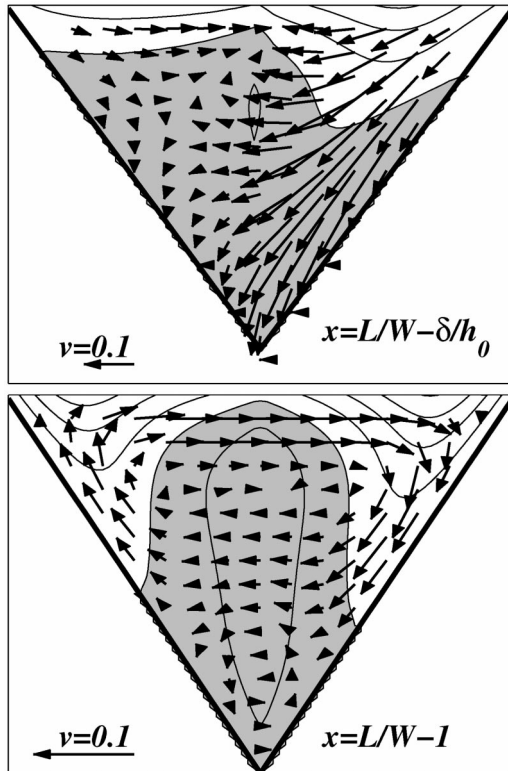


FIG. 13. Velocity sections for $\delta^{-1} = 6$ at two locations near the $+x$ end of the basin ($L = 5$), as marked on the right-hand panel of Fig. 7: $x = 4$ and (bottom) $x = 5 - \delta/h_0$. The axial velocity is negative in the shaded areas, and the axial-velocity contour interval is 0.05. Lateral and vertical velocities (v and w) are represented by vectors. The lateral velocity scale is different in each frame.

the central part of the basin to this area arrives near the surface and is swept down and toward the center, where it reverses direction and moves back upwind.

8. Trajectories

Fluid parcel trajectories are determined by integrating the three components of velocity with respect to time. The trajectories of two different parcels released on the central section ($x = 0$) of the elongated ($L = 5$) basin described above, for $\delta^{-1} = 6$, are illustrated in Fig. 14. The parcel whose trajectory is illustrated in the top row was initially located at $y = 0.5$ and $z = -0.025$. The parcel illustrated in the bottom row was located at $y = 0.25$ and $z = -0.05$. The complete trajectory of each parcel consists of two legs, one for which the overall drift is downwind (represented by the heavy trace) and the other for which the overall drift is upwind.

The downwind trajectories of both parcels are qualitatively similar. The parcels spiral in toward the close end, confined in a sheath on the outer periphery of the near-surface gyre. The velocity is positive (downwind) when the parcel is near the sides or the surface and is negative (upwind) when the parcel is crossing the basin

in the interior. The number of circuits a particle undergoes before reaching the closed end varies, depending on the proximity to the surface at the initial position: parcels that are released very close to the surface generally have larger average axial velocities (consistent with the axial velocity distributions illustrated in Figs. 10 and 13) than do particles released closer to the bottom.

There are two separate upwind paths. After turning at the closed end, some particles become entrained in the core portion of the upper gyre and drift upwind from the end with the same sense of rotation (in lateral sections) as the inbound flow. Other parcels are swept into the bottom Ekman layer near the closed end and become entrained in the lower gyre, where they drift upwind, rotating in the opposite sense from the other particles.

9. Discussion

Even moderate rotation profoundly affects the wind-driven circulation, qualitatively and quantitatively. In the steady model described here, the solutions are dependent on δ , the ratio of the Ekman layer depth to the maximum depth h_0 , or, equivalent, on the Ekman number. The Ekman depth is a function of the eddy viscosity and typically is of order 10 m. This study demonstrates that rotation needs to be included in models of wind-driven circulation where the maximum depth is of that order or larger. In an unsteady flow, the Ekman solutions are attained after transients die off, in a time of order f^{-1} . If the wind forcing varies markedly over time scales shorter than a day, rotation can be assumed not to affect the flow. This model excludes advective processes. The importance of advection relative to rotation is measured by the Rossby number, $Ro = u^*/fL$, if L is a characteristic horizontal scale. If the wind-driven velocity is of order 0.1 m s^{-1} , with $f = 10^{-4} \text{ s}^{-1}$, advection is only important when the length scale is of order 1 km, although in real basins rapid changes in the topography can result in locally large values of Ro . Pedlosky (1974) shows that the relative amplitude of stratification to rotation is measured by the ratio $g\Delta\rho h_0/(\rho f^2 B^{*2})$, where $\Delta\rho$ is the relative vertical density difference. If the basin half-width B^* is taken as 2 km, with $f = 10^{-4} \text{ s}^{-1}$ and $h_0 = 10 \text{ m}$, stratification becomes significant when $\Delta\rho/\rho = 4 \times 10^{-4}$. This is exceeded in all but well-mixed estuaries.

Fischer (1972) seems to have been the first to suggest that models of estuarine flow ought to be based on a model of vertical eddy viscosity that depends on local water depth, rather than being constant. Hunter and Hearn (1987) considered the vertical eddy viscosity to depend on the depth raised to different powers. Friedrichs and Hamrick (1996) compare analytical solutions with different parameterizations of K with observations of estuarine flow in the James River, and conclude that a linear dependence of eddy viscosity on local depth may be adequate for the James. This model was refor-

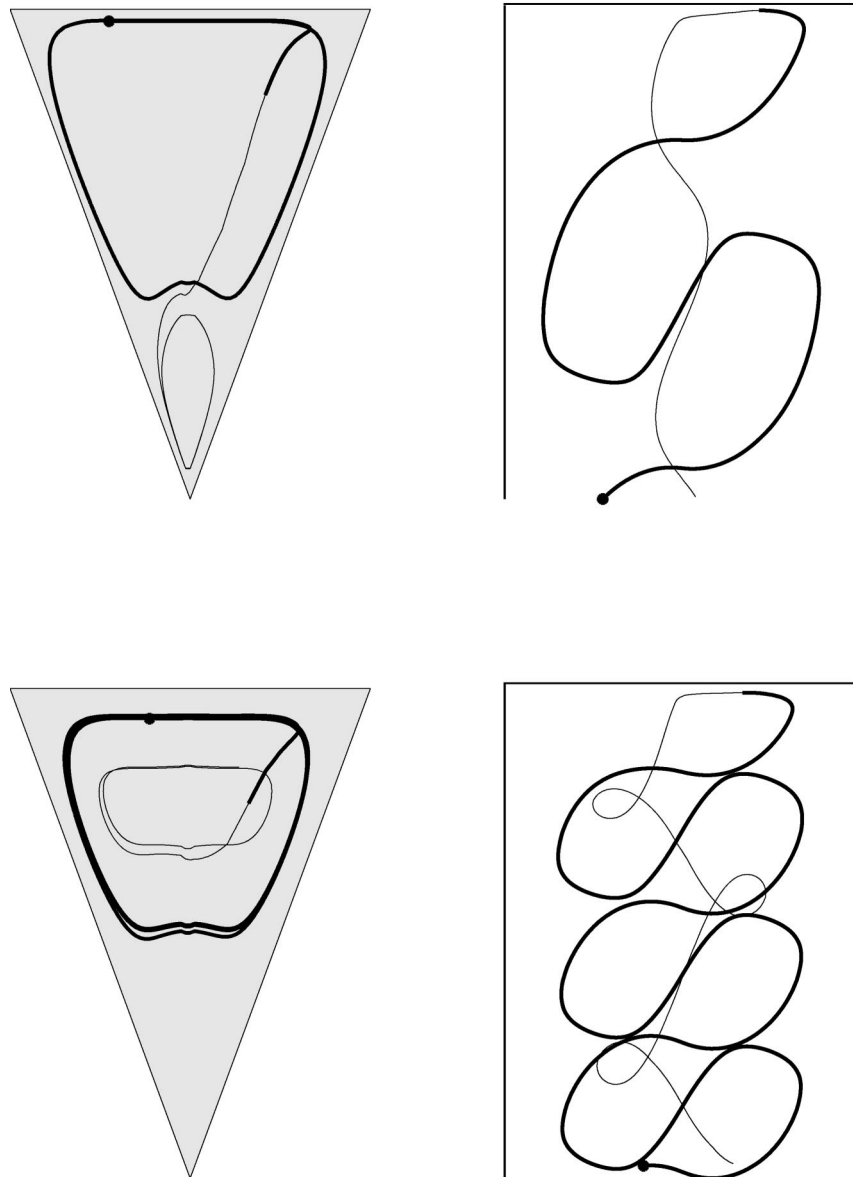


FIG. 14. Trajectories of two particles released near the surface, at the center ($x = 0$) of a basin, in the $x > 0$ section. The wind is blowing in the $+x$ direction, from the bottom of the page toward the top. (top) A parcel released at $z = -0.02$; (bottom) a parcel released at $z = -0.05$. The viewer is looking along the positive x axis, down the central axis of the basin, toward the closed end, (right) plan view, from above the basin. The solid symbol marks the release position. The heavy line indicates the trajectory from the release to the farthest inward position, and the light line marks the return trajectory.

mulated using a K that depends linearly on depth, leading to a description similar to that presented here for constant K . The results are in every way qualitatively similar to those described above and, for that reason, are not described in any detail. Using a depth-dependent K enhances velocities in the shallower portions of the basin and increases the lateral variability in the flow.

Near the middle of the basin, the three-dimensional solutions developed here are similar to the flow de-

scribed by Simons (1980). The method adopted here allows the determination of the flow in the entire basin and, in particular, in the areas near the axial ends. The qualitative difference in the flow on either side of a closed end, corresponding to Sverdrup or Stommel boundary layers, suggests that the wind-driven current can vary substantially, even with a very simple basin shape and a constant wind stress. In the Stommel boundary layer, the velocities are of similar order to the ve-

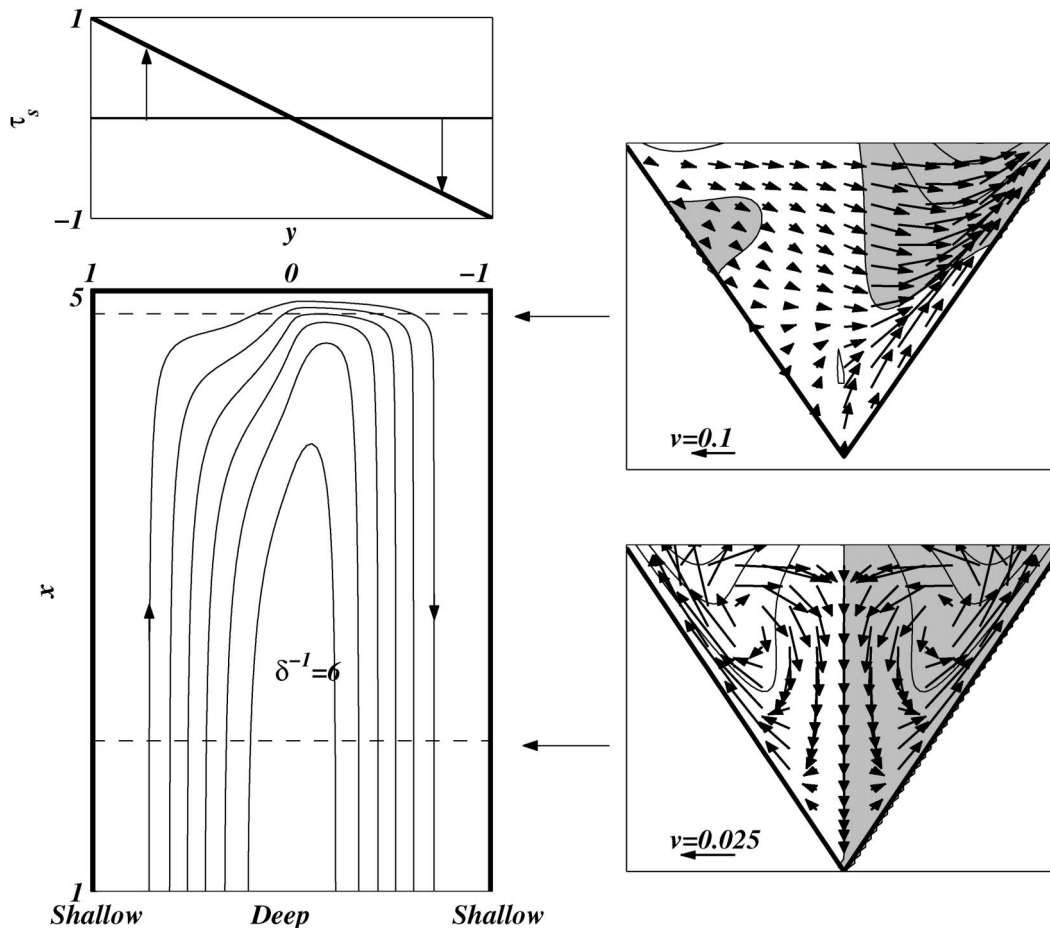


FIG. 15. Wind stress curl-driven transport streamfunction ψ for the solution to Eq. (23) for $\delta^{-1} = 6$; $L = 5$ and $h = 1 - |y|$ except within a distance of 0.25 from the ends, where the bottom shoals to zero. The section between $x = 1$ and 5 is shown. (left) The wind stress is illustrated above a plan view of the streamlines: it is applied in the x direction and varies linearly with y . The contour interval is 0.01, and the streamfunction is zero on the boundaries. (right) The velocity field in two sections that are located by the dashed lines on the streamline plan view. The convention for the velocity sections is as in Fig. 10.

locities in the case without rotation. The ratio of the velocities in the Stommel and Sverdrup boundary layers is δ^{-2} .

The solutions described to this point are all for a constant-amplitude wind parallel to the long axis of the basin. This configuration seems appropriate for lagoons and small lakes or estuaries, but the amplitude of the wind can vary as a function of position over larger basins. To describe briefly the flow that results when the wind amplitude does vary, the vertically integrated and three-dimensional flow have been computed for the same basin geometry used for the solutions displayed in Figs. 7, 10, and 13 with a constant wind stress curl, that is, where the wind amplitude varies as y . The resulting flow is illustrated in Fig. 15. With constant wind stress curl, the vertically integrated circulation consists of a single gyre (in contrast to Fig. 7), and the amplitude of the streamfunction is reduced, a consequence of the low average stress over each half-basin. With $\partial\tau_s/\partial y >$

0, upwelling takes place on both sides of the basin, and the circulation is anticyclonic. Away from the end regions, the axial pressure gradient is zero. The asymmetry between the two end regions ($y > 0$ and $y < 0$) results in a sudden acceleration of the lateral flow as it crosses from the region where $h_y < 0$ to where $h_y > 0$. Near the end ($x = 5$), the lateral flow is swift on the $h_y > 0$ side, and the convergence provides the mass required to feed the downwind flow on the negative y side of the domain.

In principle, residual flows driven by tides or by buoyancy can be derived following the procedure outlined here. For tidal flows, the forcing imparted in this analysis by the wind stress is replaced by the tidal stress produced by correlations between fluctuating sea level and bottom stress, correlations between velocity and velocity gradients, or both. For buoyancy driven flows, the variable density forces the momentum equations as shown by Kasai et al. (2000). The density field is related

to the flow through a transport equation that has to be solved with the momentum equations, as shown by Pedlosky (1974) and Hendershott and Rizzoli (1976). Both of these areas of inquiry are currently being pursued.

10. Summary and conclusions

The three-dimensional wind-driven circulation in well-mixed lakes or estuaries has been described with a linear, steady barotropic model in an elongated basin of arbitrary depth distribution on an f plane. A vorticity equation for the vertical transport streamfunction is derived first, and an analytic solution has been found for a rectangular basin in which the depth depends only on lateral position and the bottom slope does not change sign. Numerical solutions for more general basin shapes and for spatially variable winds are also presented. Without rotation, Csanady (1973) has shown that the vertically integrated transport is proportional to $\tau_s h_0^2 / (\rho K)$. Rotation is shown to limit the vertically integrated flow by a factor δ over the value without rotation. Mathieu et al. (2002) have shown that in a closed rectangular basin without rotation, the flow turns in the vicinity of the axial boundaries in regions of length comparable to the width of the basin. Here it has been shown that with rotation the flow turns in boundary layers that have different dimensions and dynamics depending on their orientation. To the left of an observer looking toward the closed end, the Sverdrup boundary layer extends to a length δ^{-1} from the wall and the flow velocities are slow. On the other side, the Stommel boundary layer extends to a length δ from the wall. This region is dynamically similar to the western boundary current in the wind-driven oceanic circulation. The identification of these miniature Gulf Streams, where the horizontal velocities are large and upwelling or downwelling is locally intense, is one of the central results of the model presented here.

The pressure field derived from the vertically integrated solutions has been used to determine the horizontal velocities at each point in the basin from the Ekman solutions, and the vertical velocities are determined by vertically integrating the continuity equation. Without rotation, only axial flow occurs away from axial boundaries, and the flow at any depth is qualitatively similar to the vertically integrated flow. With rotation, the structure of the three-dimensional flow is much more complicated and very different from the vertically integrated flow field. For a wind blowing along the axis of the basin, the near-surface lateral flow is in the sense expected from Ekman dynamics. For uniform winds, the axial pressure gradient is always an important term in the axial momentum balance. There is always an upwind interior flow near the center of the basin. Because of the finite width of the basin, the surface lateral flow is compensated by a midwater flow in the opposite direction, forming a gyre in lateral sections. In the bottom boundary layer, the interior axial flow causes a

lateral circulation in the opposite sense from the near-surface gyre: very close to the bottom, the lateral flow is in the same direction as near the surface.

Without rotation, the pattern of particle trajectories is very similar to the pattern of vertically integrated streamlines. With rotation, they are qualitatively different. Fluid parcels initially located near the surface of the basin eventually drift downwind, but their path reverses direction as they are swept through different areas of axial velocity by the lateral circulation. Near the end of the basin, parcels reverse their mean drift by either of two pathways, one near the center of the near-surface gyre, the other in the lower gyre. The much more complicated trajectories in a rotating flow are another central result of this work. They suggest that rotation should considerably increase estimates of residence times.

Acknowledgments. Thanks are given to Myrl Hendershott, Rick Salmon, Arnaldo Valle-Levinson, and Bill Young for many illuminating conversations. Jim Lerczak provided very helpful suggestions for the organization of the manuscript. I am most grateful to two anonymous reviewers who provided many helpful insights and suggested important additions to the original manuscript.

APPENDIX

The Streamfunction in the Sverdrup Boundary Layer

Equation (31) is parabolic and is similar to the equation governing the distribution of temperature in a rod of finite length (Carslaw and Jaeger 1959). The solution is found by expanding $\psi^{r,+}$ in terms of eigenfunctions:

$$\psi^{r,+} = \sum_{n=0}^{\infty} a_n Y_n(y) X_n(x^+), \quad (\text{A1})$$

where the Y_n are the solutions to the eigenvalue problem

$$Y_{nyy} + \frac{R_y}{R} Y_{ny} = \lambda_n \frac{S_y}{R} Y_n \quad (\text{A2})$$

with boundary conditions $Y_n = 0$ at $y = 0$ and 1 . The Y_n are normalized such that

$$\int_0^1 \frac{S_y Y_n Y_m}{R} dy = \text{sign}(h_y) \delta_{nm}, \quad (\text{A3})$$

where δ_{nm} is the Kronecker delta. The first four eigenvalues of Eq. (A2), for a linear dependence of h on y , are listed in Table A1 for different values of δ^{-1} , along with the amplitudes as defined by Eq. (A6). The eigenvalues vary little with δ^{-1} , and the magnitude of the amplitudes demonstrates that the lowest mode dominates the solution. The first eigenvalue is numerically close to the value π^2 given by Welander (1976).

TABLE A1. Eigenvalues and amplitudes of the first four modes for various values of δ^{-1} . The depth varies as a linear function of y .

δ^{-1}	$\lambda_1 (a_1)$	$\lambda_2 (a_2)$	$\lambda_3 (a_3)$	$\lambda_4 (a_4)$
3	10.3 (0.15)	32.5 (-0.04)	66.2 (-0.02)	111.3 (-0.01)
6	9.3 (0.27)	30.3 (0.07)	62.0 (0.04)	104.5 (-0.02)
10	10.7 (0.25)	28.6 (0.10)	59.4 (-0.05)	100.8 (0.03)
100	10.2 (0.24)	30.1 (-0.11)	60.0 (-0.07)	99.8 (-0.05)

Introducing Eq. (A1) into Eq. (31) gives

$$\begin{aligned} & \frac{S_y}{R} \sum_{n=0}^{\infty} a_n Y_n X_n' - \sum_{n=0}^{\infty} a_n X_n \left[Y_n'' + \frac{R_y}{R} Y_n'(y) \right] \\ &= \frac{1}{\delta R} \left(\frac{1}{Ph} \right)_y, \end{aligned} \quad (\text{A4})$$

where the prime denotes differentiation with respect to x^+ . The bracketed second term on the left of Eq. (A4) is evaluated with the definition in Eq. (A2) of Y_n and the resulting Eq. (A4) is multiplied by Y_m and integrated from $y = 0$ to $y = 1$:

$$\begin{aligned} & \sum_{n=0}^{\infty} a_n X_n' \int_0^1 \frac{S_y Y_n Y_m}{R} dy - \sum_{n=0}^{\infty} a_n \lambda_n X_n \int_0^1 \frac{S_y Y_n Y_m}{R} dy \\ &= \int_0^1 \frac{1}{\delta R} \left(\frac{1}{Ph} \right)_y Y_m dy. \end{aligned} \quad (\text{A5})$$

Introducing

$$a_m = \frac{1}{\lambda_m} \int_0^1 \frac{1}{\delta R} \left(\frac{1}{Ph} \right)_y Y_m dy \quad (\text{A6})$$

into Eq. (A5), along with the orthogonality condition in Eq. (A3), gives

$$\sum_{n=0}^{\infty} a_n X_n' \delta_{nm} - \sum_{n=0}^{\infty} a_n \lambda_n X_n \delta_{nm} = -a_m \lambda_m \quad (\text{A7})$$

for $h_y < 0$. Dividing Eq. (A7) by $a_m \lambda_m$ yields a first-order nonhomogeneous ordinary differential equation for the X_n :

$$\frac{1}{\lambda_n} \frac{dX_n}{dx^+} - X_n = -1. \quad (\text{A8})$$

The boundary conditions on X_n are

$$\begin{aligned} X_n &= 0 \quad \text{at } x^+ = \delta L \quad \text{and} \\ X_n &\rightarrow 1 \quad \text{as } \delta L - x^+ \rightarrow \infty. \end{aligned} \quad (\text{A9})$$

The solution of Eq. (A8) subject to Eq. (A9) is

$$X_n = 1 - e^{\lambda_n(x^+ - \delta L)} = 1 - e^{\lambda_n \delta(x-L)}, \quad (\text{A10})$$

where the constant of integration has been chosen so that $X_n = 0$ at $x^+ = L$. The dependence on $e^{\lambda_n \delta(x-L)}$, combined with the requirement that ψ remain finite in the interior, limits the utility of this solution to boundaries that are behind an observer, looking ahead with the coast on the right in the Northern Hemisphere. This limitation is an intrinsic property of the parabolic nature of Eq. (31).

REFERENCES

- Birchfield, G. E., 1967: Horizontal transport in a rotating basin of parabolic depth profile. *J. Geophys. Res.*, **72**, 6155–6163.
- Carslaw, H. S., and J. C. Jaeger, 1959: *Conduction of Heat in Solids*. 2d ed. Clarendon Press, 510 pp.
- Csanady, G. T., 1973: Wind-induced barotropic motions in long lakes. *J. Phys. Oceanogr.*, **3**, 429–438.
- , 1978: The arrested topographic wave. *J. Phys. Oceanogr.*, **8**, 47–62.
- Fausett, L. V., 1999: *Applied Numerical Analysis Using Matlab*. Prentice Hall, 596 pp.
- Fischer, H. B., 1972: Mass transport mechanisms in partially stratified estuaries. *J. Fluid Mech.*, **53**, 671–687.
- Friedrichs, C. T., and J. M. Hamrick, 1996: Effects of channel geometry on cross sectional variations in along channel velocity in partially stratified estuaries. *Buoyancy Effects on Coastal and Estuarine Dynamics*, D. G. Aubrey and C. T. Friedrichs, Eds., Coastal and Estuarine Studies, Vol. 53, Amer. Geophys. Union, 283–300.
- Hendershott, M. C., and P. Rizzoli, 1976: The winter circulation in the Adriatic Sea. *Deep-Sea Res.*, **23**, 353–370.
- Hunter, J. R., and C. J. Hearn, 1987: Lateral and vertical variations in the wind-driven circulation in long, shallow lakes. *J. Geophys. Res.*, **92**, 13 106–13 114.
- Kasai, A., A. E. Hill, T. Fujiwara, and J. H. Simpson, 2000: Effect of the earth's rotation on the circulation in regions of freshwater influence. *J. Geophys. Res.*, **105**, 16 961–16 969.
- Mathieu, P. P., E. Deleersnijder, B. Cushman-Roisin, J. M. Beckers, and K. Bolding, 2002: The role of topography in small well-mixed bays, with application to the lagoon of Mururoa. *Cont. Shelf Res.*, **22**, 1379–1395.
- Pedlosky, J., 1974: On coastal jets and upwelling in bounded basins. *J. Phys. Oceanogr.*, **4**, 3–18.
- Pritchard, D., 1967: Observations of circulation in coastal plain estuaries. *Estuaries*, G. H. Lauff, Ed., American Association for the Advancement of Science, 37–44.
- Simons, T. J., 1980: Circulation models of lakes and inland seas. *Can. Bull. Fish. Aquat. Sci.*, **203**, 1–146.
- Stommel, H., 1948: The western intensification of wind-driven ocean currents. *Trans. Amer. Geophys. Union*, **29**, 202–206.
- Valle-Levinson, A., C. Reyes, and R. Sanay, 2003: Effects of bathymetry, friction, and rotation on estuary–ocean exchange. *J. Phys. Oceanogr.*, **33**, 2375–2393.
- Welander, P., 1968: Wind-driven circulation in one- and two-layer oceans of variable depth. *Tellus*, **20**, 2–15.
- , 1976: A zonally uniform regime in the oceanic circulation. *J. Phys. Oceanogr.*, **6**, 121–124.
- Wong, K. C., 1994: On the nature of transverse variability in a coastal plain estuary. *J. Geophys. Res.*, **99**, 14 209–14 222.